

Ultra Low Noise Preamplifier Design for Magnetic Particle Imaging

Quincy Huynh



Electrical Engineering and Computer Sciences
University of California at Berkeley

Technical Report No. UCB/EECS-2018-42

<http://www2.eecs.berkeley.edu/Pubs/TechRpts/2018/EECS-2018-42.html>

May 10, 2018

Copyright © 2018, by the author(s).
All rights reserved.

Permission to make digital or hard copies of all or part of this work for personal or classroom use is granted without fee provided that copies are not made or distributed for profit or commercial advantage and that copies bear this notice and the full citation on the first page. To copy otherwise, to republish, to post on servers or to redistribute to lists, requires prior specific permission.

Acknowledgement

I could not have done this without the help of Professor Steven Conolly, Caylin Vanhook, Xinyi Zhou, Bo Zheng and the other members of the Berkeley Imaging Systems Laboratory. I want to also say thanks to my parents for all the sacrifices they have made and the hard work they have done to provide me the opportunity to go to UC Berkeley for undergraduate and graduate school and overall live a better life. Con yêu mẹ và bố.

Ultra Low Noise Preamplifier Design for Magnetic Particle Imaging

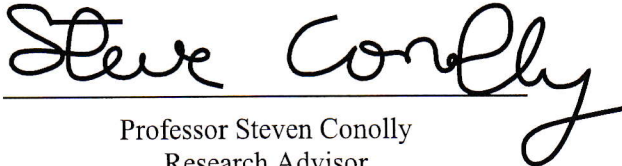
by Quincy Le Huynh

Research Project

Submitted to the Department of Electrical Engineering and Computer Sciences,
University of California at Berkeley, in partial satisfaction of the requirements for the
degree of **Master of Science, Plan II.**

Approval for the Report and Comprehensive Examination:

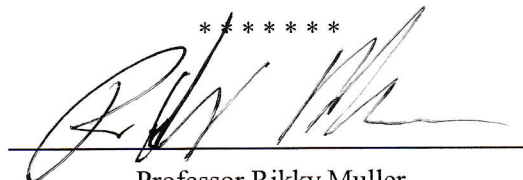
Committee:



Professor Steven Conolly
Research Advisor

May 10, 2018

(Date)



Professor Rikky Muller
Second Reader

May 10, 2018

(Date)

Abstract

Ultra Low Noise Preamplifier Design for Magnetic Particle Imaging

by

Quincy Le Huynh

Master of Science in Electrical Engineering and Computer Science

University of California, Berkeley

Professor Steven Conolly, Chair

Diagnostically relevant medical imaging systems require high signal to noise ratio (SNR) for high fidelity. Tracer modalities, such as Magnetic Particle Imaging (MPI), must have high SNR for excellent detection sensitivity. Stem cell scientists and physicians would prefer to see even a single stem cell inside the body, but all conventional whole-body imaging methods today are limited to 10,000-cell sensitivity. Recent publications in Professor Steven Conolly's lab demonstrated 200-cell sensitivity with MPI, and that was performed without ultra-low noise preamps. In this report, I will present techniques to design an ultra low noise wideband preamplifier for MPI applications, specifically for the arbitrary waveform relaxometer (AWR) used in the Professor Conolly's Berkeley Imaging Systems Laboratory (BISL). The AWR is used to characterize magnetic particles and optimize MPI drive waveforms for *in-vitro* biosensing and *in-vivo* imaging with MPI. Wideband low noise design requires many considerations, e.g. bandwidth, averaging, and input stage topologies. For each technique presented, I will discuss advantages and disadvantages, thus emphasizing the end goal of designing a wideband preamplifier with the ultimate goal of reaching a possible 1-5 cell sensitivity physical limit for MPI.

Table of Contents

Contents	i
Figures	iv
1 Introduction	1
1.1 Magnetic Particle Imaging	1
1.2 Motivation for Preamplifier	4
2 Electrical Model of Solenoid Inductive Sensor	6
2.1 Solenoidal Inductor Model	6
2.2 MPI Signal at the Receiver	8
3 Noise in MPI Systems	9
3.1 Body Noise	9
3.2 Thermal Noise	10
3.3 Preamplifier: Field Effect Transistor Device Noise	10
3.4 Preamplifier: Two Port Model Noise	11
3.5 Noise Performance Metrics	12
3.6 Optimal Noise Figure	13
3.7 Signal-to-Noise Ratio in MPI	15
4 Optimal Noise Matching	16
4.1 Transformer Matching	16
4.2 LC Matching Networks	17
4.3 Parallel LNA Devices	19

4.4	Bandwidth Limits on Matching Networks	20
5	Ultra Low Noise Preamplifier Analysis and Design	21
5.1	Device Choices	21
5.2	Cascode Topology	22
5.3	Negative Feedback Effects on Noise	22
5.4	Proposed Design: AC Analysis	23
5.5	Proposed Design: Stability Analysis	26
5.6	Proposed Design: Noise Analysis	27
5.7	Proposed Design: Noise Matching	28
5.8	Comparison to Previous Preamplifiers	30
6	Conclusion	32
6.1	Motivation and Big Picture	32
6.2	Future Work	32
	References	33

List of Figures

1.1	MPI/CT Images of Mice for Various Applications	2
1.2	BISL FFP and FFL Scanners	2
1.3	Langevin Function	4
1.4	Point Spread Function	4
1.5	Two Particles In Space	4
1.6	Two Particles in Time	4
2.1	Circuit Model of Receive Coil	6
3.1	Two Port Noise Model Resistive Sensor	12
3.2	Two Port Noise Model with Inductive Sensor	14
4.1	Transformer Model with Primary and Secondary Impedances	16
4.2	Simple LC Matching Network	17
4.3	Two Section LC Network	18
4.4	Summing Amplifier	19
5.1	JFET Cascode	22
5.2	Shunt-Series Resistive Feedback	22
5.3	Proposed Preamplifier Design	24
5.4	Open Loop Gain	25
5.5	Open Loop Phase	25
5.6	Closed Loop Gain	25
5.7	Closed Loop Phase	25
5.8	Loop Gain Stability Testbench	26

5.9	Loop Gain Stability	26
5.10	Input Referred Noise with Zero Source Resistance	27
5.11	Noise Figure with No Matching	27
5.12	Input Referred Noise with Transformer Matching	29
5.13	Noise Figure with Transformer Matching	29
5.14	Input Referred Noise with Parallel Preamps and Transformer Matching . . .	30
5.15	Noise Figure with Parallel Preamps and Transformer Matching	30

Chapter 1

Introduction

1.1 Magnetic Particle Imaging

Magnetic Particle Imaging (MPI) is a new tracer-based molecular imaging technique that detects and quantifies the intense magnetization of superparamagnetic iron oxide (SPIO) tracers in the body [1]. Tracer imaging modalities are usually functional imaging modalities that employ a tracer such as radioactive labels, or in MPI's case, a magnetic nanoparticle. This unique contrast mechanism, combined with its use of low-frequency magnetic fields and clinically safe magnetic tracers, enables MPI to produce clinical-grade images with zero tissue signal attenuation, high contrast-to-noise ratio, and high sensitivity, all with a better safety profile than nuclear medicine. Like Magnetic Resonance Imaging (MRI), MPI is bound by Magnetostimulation and Specific Absorption Rate (SAR) safety limitations. Since it is a tracer modality, MPI is best compared to other gold-standard tracer imaging techniques, such as nuclear medicine (PET, SPECT and scintigraphy). However, MPI has no radiation dosage. Applications of MPI include angiography, strokes, stem cell tracking, lung perfusion imaging, traumatic brain injury imaging, white blood cell tracking, and gastrointestinal bleed imaging among many other highly critical medical imaging applications [2–8]. Examples are shown in Figure 1.1. Tracer imaging modalities like Positron Emission Tomography (PET) only give an image of the tracer distribution, with no anatomic information. PET images are often paired with anatomical imaging modalities such as Computed Tomography (CT) to give an anatomical reference [9]. Like PET/CT, we sometimes pair MPI with CT as an anatomical reference.

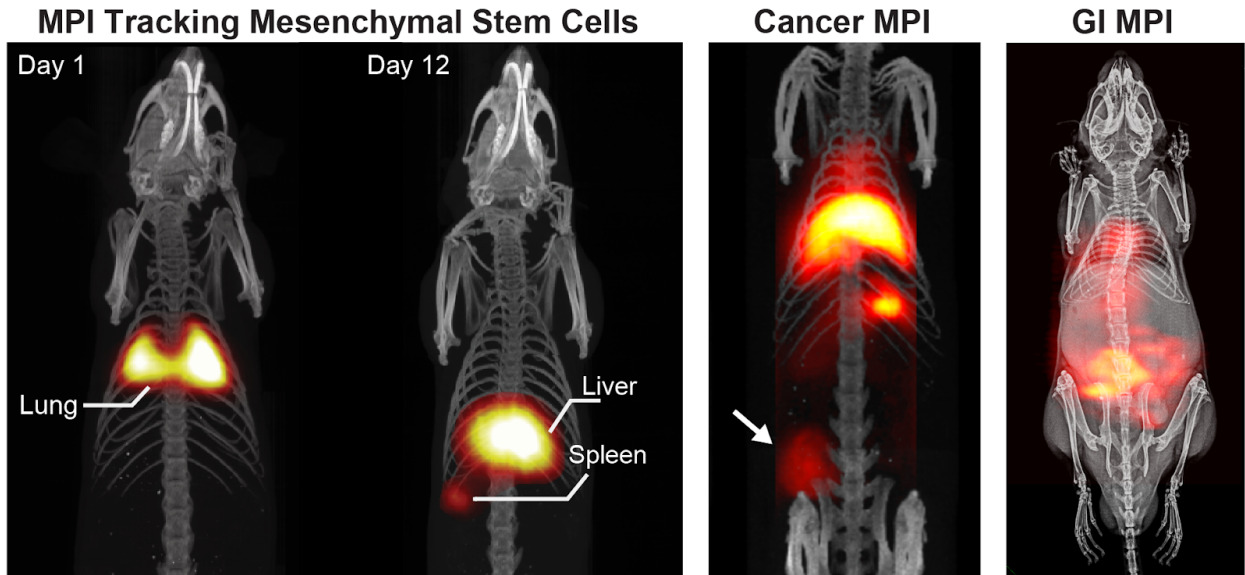


Figure 1.1: MPI/CT Images of Mice for Various Applications. Since MPI is a tracer modality is often co-registered to an anatomic reference scan like CT, X-ray, or MRI. Multimodality imaging techniques provides morphofunctional information to clinicians and researchers in a way that couldn't be done with just one modality [10].

MPI works by constructing a magnetic gradient field with a field free region (FFR) using a magnet with a gradient G (units of [T/m]). The FFR can be a point (FFP) or a line (FFL). The Berkeley Imaging Systems Laboratory currently has one of each type of scanner shown in Figure 1.2.

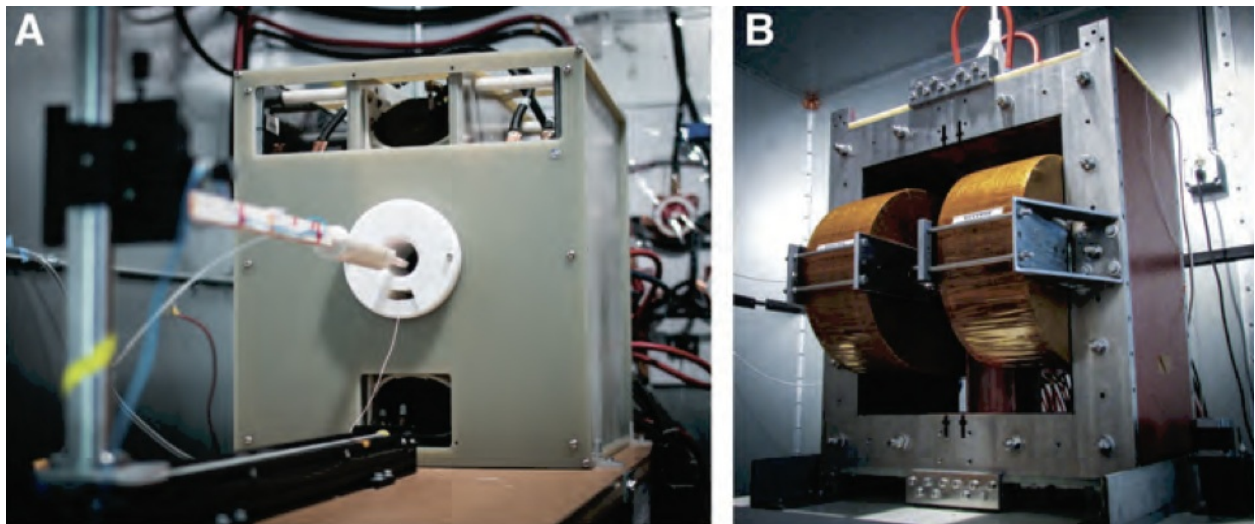


Figure 1.2: BISL's FFP and FFL Scanners. A) 7 T/m Gradient FFP (Gertrude) and B) 6.3 T/m Gradient FFL (Helga). Built by researchers in BISL, these two scanners were the first MPI scanners built in North America. They were built for murine (mice) imaging experiments.

The FFR is where the magnetic field $H(x, t) = 0$. As the field free region crosses the magnetic particle, its magnetization changes, which induces a voltage signal that we then amplify and send to our data converter using the principle of reciprocity shown by Hoult et al. [11].

$$\zeta = -\mathbf{B} \frac{\partial \mathbf{m}}{\partial t} \quad (1.1)$$

where \mathbf{B} is the field that is generated by the coil per unit current (units of T/A) and \mathbf{m} is

the magnetic moment of the magnetic nanoparticle (units of $\text{A}\cdot\text{m}^2$).

We scan an image by driving a Helmholtz coil, thus moving the FFR by applying a time varying homogeneous offset field $H_0(t)$.

$$H(x, t) = H_0(t) - Gx \tag{1.2}$$

We can solve for where this FFR is by solving for x when $H(x, t) = 0$ and rewriting the equation for the magnetic field at a given point in space.

$$x_{FFR}(t) = G^{-1}H_0(t) \implies H(x, t) = G(x_{FFR}(t) - x) \tag{1.3}$$

The knowledge of where the instantaneous FFR is at any given time allows us to reconstruct the image by mapping the voltage time domain signal back to a spatial grid. In an ideal medical imaging system, a single point source (e.g., a small amount of nanoparticles) should yield an impulse at the output. In actuality, the impulse response or point spread function (PSF) is a blur that can be characterized with some full width half max (FWHM) to determine the resolution of the image. The change in magnetization of the magnetic particle is accurately described by the Langevin function which looks like a sigmoid, shown in Figure 1.3. The magnetization as a function of the applied field H is

$$M(H) = Nm\mathcal{L}(kH) \tag{1.4}$$

where N is the number of particles, m is the magnetic moment of a spherical particle, k is a property of the magnetic nanoparticle, and \mathcal{L} is the Langevin function.

$$\mathcal{L}(kH) = \frac{1}{\tanh(kH)} - \frac{1}{kH} \tag{1.5}$$

Its derivative is a well-behaved function that describes the change in magnetic flux and therefore is the PSF of the basic MPI system, shown in Figure 1.4.

$$\frac{d\mathcal{L}(kH)}{d(kH)} = \frac{1}{(kH)^2} - \frac{1}{\sinh^2(kH)} \tag{1.6}$$

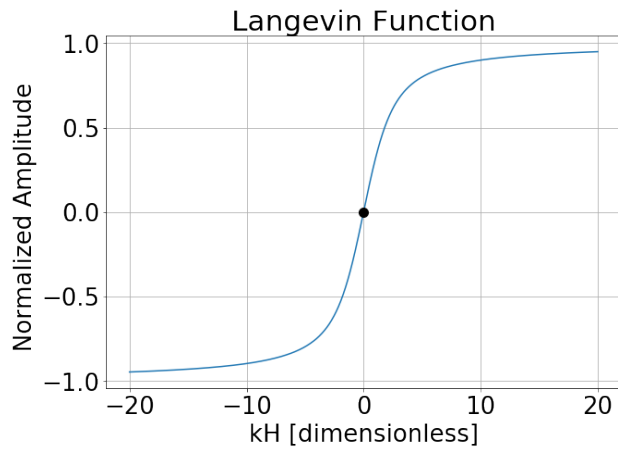


Figure 1.3: Langevin Function

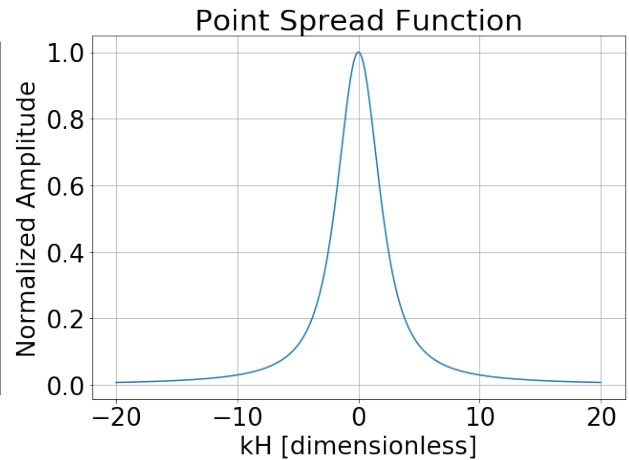


Figure 1.4: Point Spread Function

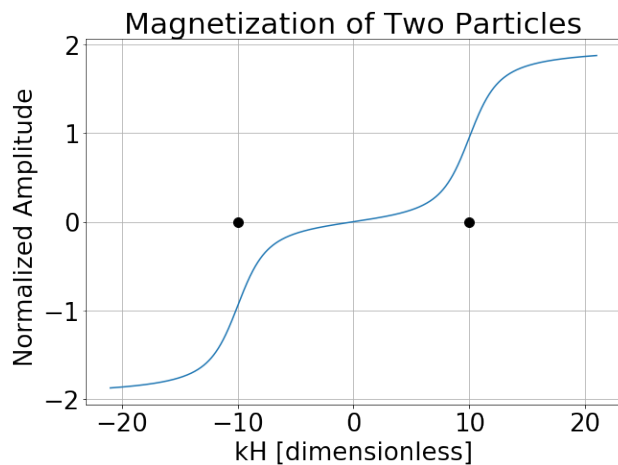


Figure 1.5: Two Particles In Space

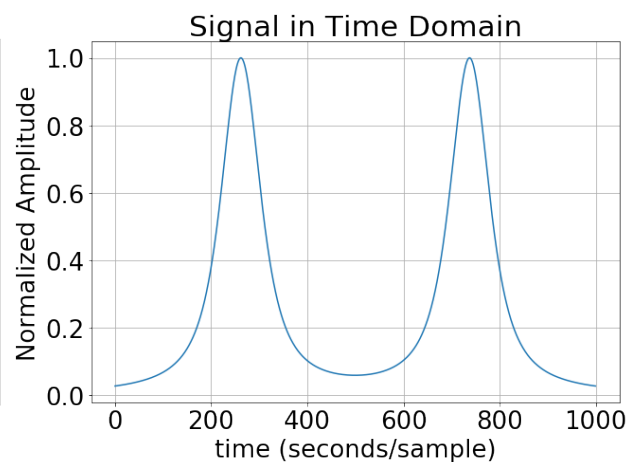


Figure 1.6: Two Particles in Time

Since the behavior of the changing magnetization of particles due to the moving FFR and the locations of the particles in x -space can be modeled as a convolution, MPI is a Linear and Shift Invariant system (LSI) [13].

$$s(t) \propto \rho(x) * h(x) \Big|_{x=x_{FFR}} \quad (1.7)$$

Where $h(x) = \frac{\partial \mathcal{L}(Gx/H_{sat})}{\partial x}$ (Langevin derivative evaluated at the FFR) and $\rho(x)$ is the particle distribution in space [particles/m].

For example, if the system encounters two particles during the scan spaced apart by some length, the magnetization will be similar to what is shown in Figure 1.5 and the signal in the time domain will be read out as shown in Figure 1.6.

1.2 Motivation for Preamplifier

Goodwill et. al shows that the resolution, bandwidth and SNR of a MPI system is dependent only on the scanning speed, gradient strength and SPIO langevin saturation curve [12]. Scanning speed and gradient strength are both limited by human safety concerns (dB/dt

and SAR, [14]) and cannot be significantly increased. However MPI researchers still resort to using SPIOs optimized for Magnetic Resonance Imaging (MRI) since MPI-tailored SPIOs are not yet available. The most important tool for developing new SPIOs for MPI is the Relaxometer [15–17].

In the Berkeley Imaging Systems Laboratory, Zhi Wei Tay built the arbitrary waveform relaxometer (AWR), an apparatus that can be used to characterize magnetic particles and optimize the excitation/drive waveforms. The AWR accomplishes this through a wideband excitation (DC-400 kHz) [17]. The source of the signal is an inductive sensor.

Zheng et. al presented several techniques for optimal broadband noise matching for inductive sensors which we will discuss and employ in our low noise preamplifier design. These techniques include transformer matching networks, parallel devices and number of coil windings of the receive coil [18]. It is important to maintain a low noise figure in the wide band of excitation frequencies used in the AWR so that we can characterize magnetic particles and optimize their excitation schemes with high fidelity.

In the next chapters, we first describe a model for the MPI receive coil as a sensor and a model of noise in the MPI systems. we then develop a design for a preamplifier for the receive chain for the sensor.

Chapter 2

Electrical Model of Solenoid Inductive Sensor

2.1 Solenoidal Inductor Model

The model of the MPI system is an inductively coupled transmit and receive coil with the subject placed inside the coils. For BISL's scanners, the coil bore size is 56 mm in diameter, which is big enough to fit mice. The AWR receive coil bore size is 6 mm, which is big enough to fit in a tube with particle samples for characterization.

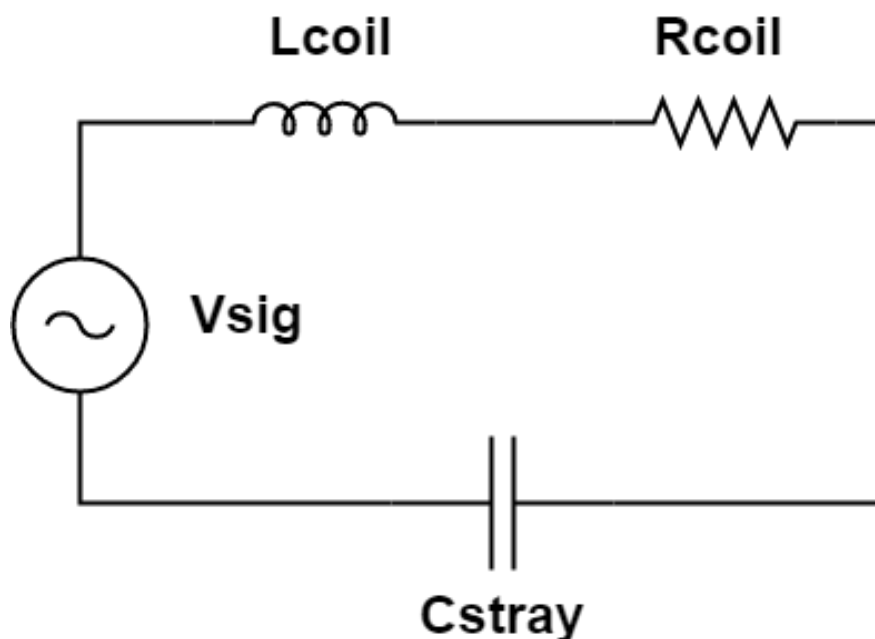


Figure 2.1: Circuit Model of Receive Coil

The transmit coil drives an excitation waveform that changes the magnetization of the magnetic particle tracers. The change in magnetization induces a voltage that is picked up by the receive coil. We can represent the signal as a voltage source in series with an inductor and coil winding resistance in parallel with a stray capacitance due to the capacitance between

turns. An equivalent circuit model is shown in Figure 2.1.

The equations for each part of the models are well defined. The inductance of a single layer solenoid is a function of its geometry [19].

$$L_{coil} = \frac{\mu N^2 A}{l} \quad (2.1)$$

where μ is the permeability of the core material (in MPI, the core material is animal tissue (mainly water), which has a -9 ppm magnetic susceptibility whereas air has ± 0.16 ppm [20]); N is the number of turns in the coil; A is the cross sectional area of a turn; and l is the length of the solenoid.

The coil winding DC resistance is simply the resistance of a conductor

$$R_{coil} = \rho \frac{l}{A} \quad (2.2)$$

where ρ is the resistivity of the conductor, which is copper in our case. l is the length of the overall wire if unwound. A is the cross section of the wire, which can be determined by the wire gauge.

However, since we are working at AC frequencies, the skin effect will decrease the effective cross sectional area of the wire, since at higher frequencies, since currents create eddy currents that effectively causes current crowding, often to the periphery of the conductor [21].

The stray capacitance of a single layer solenoid comes from the turn-to-turn capacitances, which are the equivalent capacitances between two corresponding points of any pair of adjacent turns [22]. The overall stray capacitance is then

$$C_{stray} = \frac{C_t}{N - 1} \quad (2.3)$$

where C_t is the turn-to-turn capacitance and N is the number of turns. The turn-to-turn capacitance was derived in Grandi et al. as

$$C_t = \frac{\pi^2 D \epsilon_0}{\ln(p/2r + \sqrt{(p/2r)^2 - 1})} \quad (2.4)$$

where r is the wire radius, p is the winding pitch (same units as r and D), D is the turn diameter, and ϵ_0 is the permittivity of free space [22].

The stray capacitance is fairly small (on the order of femtoFarads) compared to the input capacitance (C_{in}) of the preamplifier which is on the order of picoFarads, which will dominate

our resonant frequency. The resonant frequency of the receive circuit is then

$$f_{res} = \frac{1}{2\pi\sqrt{L_{coil} \cdot (C_{in} + C_{stray})}} \quad (2.5)$$

The winding resistance sets the Q factor of the resonance.

$$Q = \frac{\omega_{res}L_{coil}}{R_{coil}} = \frac{1}{\omega_{res}R_{coil}(C_{in} + C_{stray})} \quad (2.6)$$

2.2 MPI Signal at the Receiver

The induced emf at the detector coil can be written as a function of the field that is generated by the coil per unit current. This is the principle of reciprocity shown by Hoult et al. [11].

$$\zeta = -\mathbf{B} \frac{\partial \mathbf{m}}{\partial t} \quad (2.7)$$

where \mathbf{B} is the field that is generated by the coil per unit current (units of T/A) and \mathbf{m} is the magnetic moment of the magnetic nanoparticle (units of A·m²). The field generated by the coil scales linearly with the number of turns N by Amperes's Law [23]. The inductance of the coil scales quadratically with N as previously shown and the winding copper resistance scales linearly with N . The copper resistance of the coil adds noise, which we will discuss in the chapter on noise in MPI.

Chapter 3

Noise in MPI Systems

Noise is a stochastic process in all information systems. Noise can be modeled with a distribution such as a gaussian distribution and described with its power spectral density, which is the power of noise at a particular frequency.

There are three sources of noise for an MPI system: thermal noise from the winding resistance of the receive coil, noise from amplifiers in the receive chain and body noise. A long-standing goal of all MPI ultra-low noise front ends is to ensure coil noise dominance since body noise dominance is not yet achievable (explained in "Body Noise"). While Zheng et al published a promising design methodology, this remains an open and crucial challenge in the MPI field [18]. Since we work at generally lower frequencies for MPI, the receive (RX) coil noise and preamp noise dominate our SNR. By designing a preamplifier with excellent noise figure, our goal is to make the noise due to the preamplifier sufficiently below the noise due to the RX coil. Our goal is then a noise figure of no more than 1 to 2 dB (noise figure is explained in "Noise Performance Metrics").

In this chapter, we will discuss the origins of each source of noise with particular emphasis on the preamplifier noise, which we will show as a two port noise model and device noise model.

3.1 Body Noise

Body noise in Magnetic Resonance Imaging (MRI) is shown to be due to Brownian thermal currents in the 310K body, which induce voltage noise in the receiver coil [24]. Macovski shows that this noise standard deviation is proportional to the square of the radius of the

body, the square root of the length of the body and the square of the frequency.

$$\sigma_n = \frac{\omega\mu_0 N r_0^2}{2} \sqrt{\frac{kTl}{\rho l}} \quad (3.1)$$

Where r_o is the radius of the body (m), l is the length of the body (m), and ω is frequency (radians/sec). [24]. This noise is similar in MPI signals . However, body noise is not yet the dominant noise source in MPI as it currently is in MRI due to the lower frequencies used since we have not yet achieved coil resistance noise dominance.

3.2 Thermal Noise

Since body noise dominance cannot be achieved yet, our goal is to make the dominant noise source be the thermal noise due to the RX coil's resistance. Thermal noise, often called Johnson-Nyquist noise, is electronic noise generated by the thermal agitation of the charge carriers (usually the electrons) inside an electrical conductor at equilibrium. Johnson was able to show that the noise added to a system due to a conductor was dependent on the Boltzmann's constant k , bandwidth (Δf), temperature in Kelvin (T) and the conductor's resistance (R) [25].

$$\overline{V^2}/\delta f = 4kTR \quad (3.2)$$

Therefore, as bandwidth, temperature and resistance go up, the noise variance of this random process will go up. This presents a challenge for coil design winding (resistance) and in broadband MPI (bandwidth). In the future, the temperature issue can be resolved by using super cooling systems to push the coil temperature extremely low.

One assumption we've made is that the coil thermal noise is white and flat for simplicity. However, due to the inductance of the coil, capacitance of the coil, and input capacitance of the amplifier, the noise is actually shaped by the transfer function. This is called the power spectral density of the noise.

$$\overline{v_{n,tot}^2} = \overline{v_{n,R}^2} \int_0^\infty |H(f)|^2 df \quad (3.3)$$

3.3 Preamplifier: Field Effect Transistor Device Noise

Field effect transistors in amplifiers are often modeled with three types of noises, the drain current noise (or channel thermal noise), flicker noise (or $1/f$ noise), and shot noise (or

Poisson noise) [27]. The channel thermal noise arises from the fact that the channel of a FET device is a conductor and therefore must generate noise. The channel noise equation can be written as

$$\overline{i_d^2} = 4kT\gamma g_{ds,0}\Delta f \quad (3.4)$$

where γ is a fitting parameter (usually $2/3$ for long channel devices) and $g_{ds,0}$ is the channel transconductance (usually the same as g_m). This can be shown by taking the partial derivative of the drain current with respect to the drain-source voltage and plugging in $V_{DS} = 0$.

$$\begin{aligned} g_{ds,0} &= \left. \frac{\partial I_{DS}}{\partial V_{DS}} \right|_{V_{DS}=0} \\ g_{ds,0} &= \mu C_{ox} \frac{W}{L} (V_{GS} - V_{th}) = \frac{2I_{d,sat}}{V_{ov}} \end{aligned} \quad (3.5)$$

$$g_{ds,0} = g_m$$

Another source of noise comes from the fact that there are N-doped and P-doped regions in the device, creating PN junctions. Anytime that DC current flows through P-N junctions, there is shot noise that can be quantified in the following equation.

$$\overline{i_q^2} = 2qI_{dc}\Delta f \quad (3.6)$$

In particular for a junction FET (JFET), the shot noise is present due to the gate leakage current flowing from the gate to the channel, which is a PN junction. This can be represented as a function of the real part of the JFET's input gate conductance Y_{11} .

$$\overline{i_g^2} = 2qI_G\Delta f = 4kT[\text{Re}(Y_{11})] \quad (3.7)$$

3.4 Preamplifier: Two Port Model Noise

We can model the preamplifier in the receive chain as a noiseless amplifier with its input referred voltage and current noise. These noise values are usually given as noise standard deviations (e_n is in units of $\text{nV}/\sqrt{\text{Hz}}$ and i_n is in units of $\text{pA}/\sqrt{\text{Hz}}$) on datasheets for amplifiers. Voltage noise dominates for low source impedance and current noise dominates for high source impedance. Having both is crucial for accurately characterizing how much noise the amplifier adds to the signal. It is conventional to refer the noise generated by the amplifier from the output back to the input since the gain of the amplifier can vary. Since the voltage noise and current noise are linear combinations of the noise sources of the devices

and conductors inside the amplifier, they are correlated with each other.

$$\overline{e_{n,i}^2} = |Z_{corr}|^2 \overline{i_{n,i}^2} \quad (3.8)$$

However, for simplicity, it is common to treat the input referred voltage and current noise as uncorrelated sources. The variance of uncorrelated random variables is the sum of their individual variances. Even though our source impedance is inductive we will first consider a resistive source for simplicity. Consider the input of a system shown in Figure 3.1 that contains noise from the source and the input referred noise sources from the amplifier.

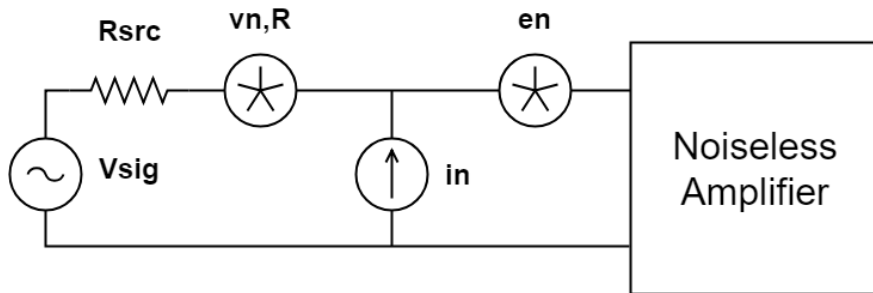


Figure 3.1: Two Port Noise Model Resistive Sensor

By superposition, we can find the overall voltage noise variance that shows up across the input of the preamplifier. This is calculated to be:

$$\overline{v_{n,tot}^2} / \Delta f = 4kTR_{src} + e_n^2 + i_n^2 R_{src}^2 \quad (3.9)$$

For a source impedance that is not purely real, the voltage noise variance is

$$\overline{v_{n,tot}^2} / \Delta f = 4kT[\text{Re}(Z_s)] + e_n^2 + i_n^2 |Z_s|^2 \quad (3.10)$$

3.5 Noise Performance Metrics

One metric that measures the noise performance of an amplifier is the Noise Figure or Noise Factor, which is defined to be the factor of how much the SNR is degraded. This can be expressed as the ratio of the SNR at the input over the SNR at the output or as the ratio of the total noise variance of the system over the noise variance due to just the source.

$$NF = \frac{SNR_{in}}{SNR_{out}} = \frac{\sigma_{n,tot}^2}{\sigma_{n,src}^2} \quad (3.11)$$

The Noise Figure for the amplifier in the previous section can then be written as:

$$NF = \frac{4kTR_{src} + e_n^2 + i_n^2 R_{src}^2}{4kTR_{src}} = 1 + \frac{e_n^2 + i_n^2 R_{src}^2}{4kTR_{src}} \quad (3.12)$$

We note that this expression is always greater than or equal to 1, implying that the SNR at a particular frequency can never get better through amplification and that amplifying our signal with noisy amplifiers only serves to hurt the signal's integrity. However, avoiding amplification is not feasible; we need the amplifier to boost the signal to within a full scale range so that an analog-digital converter (ADC) can reasonably digitize our signal. We can only afford a small degradation in SNR, so the preamp design is crucial.

The effect of noise added in subsequent stages is reduced by the factor of the gain of the stage before it. This is demonstrated by the Friis' Noise Figure of a Cascaded System with n stages [26]. This is the reason why careful design is essential for the preamplifier, since it is the first amplifier in the receive chain. The preamplifier is also usually a low noise amplifier (LNA) because of this.

$$F_{tot} = F_1 + \frac{F_2 - 1}{G_1} + \frac{F_3 - 1}{G_1 G_2} + \frac{F_4 - 1}{G_1 G_2 G_3} + \dots + \frac{F_n - 1}{\prod_{i=1}^{n-1} G_i} \quad (3.13)$$

If we let F_1 be the noise figure of our preamplifier and consider the noise figure of the rest of the cascade F_{rest} , we can rewrite this equation as

$$F_{tot} = F_{preamp} + \frac{F_{rest} - 1}{G_{preamp}} \quad (3.14)$$

This means that if the preamplifier has large gain, then it roughly sets the overall noise factor of the system and therefore sets how much SNR we lose.

3.6 Optimal Noise Figure

Since the noise figure of the preamp is dependent on R_{src} , if we consider the source resistance R_{src} to be a free variable, then we can find the R_{src} at which the noise figure is minimized. First, let's consider two notional values inherent to the preamp: its "noise power" $p_n = e_n \cdot i_n$ (units of W/Hz) and "noise impedance" $R_n = \frac{e_n}{i_n}$ (units of Ω) where e_n and i_n are the voltage and current noise density standard deviations of the preamp. In actuality for a given coil and our preamplifier, the free variable is actually the ratio of e_n and i_n , which we called R_n . This derivation is to show that the lowest noise figure achievable for a system is when the source resistance R_{src} is matched to the noise resistance R_n . We maintain the product p_n but can freely change the ratio of e_n/i_n .

From our noise figure equation, we manipulate e_n and i_n into p_n and R_n .

$$\begin{aligned}
 NF &= 1 + \frac{\frac{e_n^2}{i_n^2} + R_{src}^2}{4kTR_{src}} \cdot i_n^2 \\
 NF &= 1 + \frac{\frac{e_n^2}{i_n^2} + R_{src}^2}{4kTR_{src}} \cdot \frac{e_n}{i_n} \cdot e_n i_n \\
 NF &= 1 + \frac{R_n^2 + R_{src}^2}{4kTR_{src}R_n} \cdot p_n
 \end{aligned} \tag{3.15}$$

From there, we take a partial derivative with respect to R_n and set the derivative to 0 and solve for R_n .

$$\begin{aligned}
 \frac{\partial NF}{\partial R_{src}} &= \frac{p_n}{4kT} \frac{2R_{src}(R_{src}R_n) - R_n(R_n^2 + R_{src}^2)}{R_{src}^2 R_n^2} \\
 \frac{\partial NF}{\partial R_{src}} &= \frac{p_n}{4kT} \frac{2R_{src}^2 R_n - R_n^3 - R_{src}^2 R_n}{R_{src}^2 R_n^2} \\
 \frac{\partial NF}{\partial R_{src}} &= \frac{p_n}{4kT} \frac{R_{src}^2 R_n - R_n^3}{R_{src}^2 R_n^2} \\
 \frac{\partial NF}{\partial R_{src}} &= \frac{p_n}{4kT} \left(\frac{1}{R_n} - \frac{R_n}{R_{src}^2} \right) = 0 \implies R_{src} = R_n
 \end{aligned} \tag{3.16}$$

We see that the minimal noise figure occurs when $R_{src} = R_n$. We should be careful to note that this is the case for a particular pair of p_n and R_n or e_n and i_n . Plugging this critical point $R_{src} = R_n$ back into the noise figure formula,

$$\begin{aligned}
 NF_{min} &= 1 + \frac{R_n^2 + R_n^2}{4kTR_n R_n} \cdot p_n \\
 NF_{min} &= 1 + \frac{2R_n^2}{4kTR_n^2} \cdot p_n \\
 NF_{min} &= 1 + \frac{p_n}{2kT}
 \end{aligned} \tag{3.17}$$

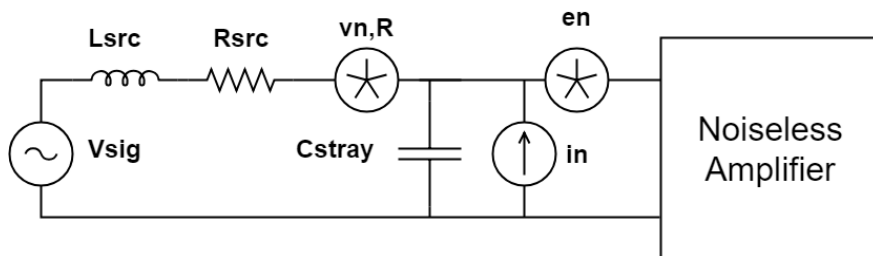


Figure 3.2: Two Port Noise Model with Inductive Sensor

As a sanity check, we confirm that kT and p_n both have a dimensionality of W/Hz which keeps NF_{min} unitless. It is important to note that the minimal noise figure depends, not on R_n , the quotient of the voltage and current noise densities, but on p_n , the product of the voltage and current noise densities e_n and i_n . This demonstrates that it is imperative to consider low input referred current noise, not just achieve low input referred voltage noise.

This is especially true when we finally put into consideration the fact that our sensor has a

reactive source impedance. We simply add the inductance of the receive coil into the noise model along with the stray capacitance, as shown in Figure 3.2. If we consider $R_{src} \rightarrow Z_{src} = R_{src} + jX_{src} = R_{src} + j\omega L_{src}$ (ignoring the very small stray capacitance), then the noise figure is then

$$\begin{aligned} NF &= 1 + \frac{e_n^2 + i_n^2 |Z_{src}|^2}{4kTR_{src}} \\ NF &= 1 + \frac{e_n^2 + i_n^2 (R_{src} + \omega^2 L_{src}^2)^2}{4kTR_{src}} \end{aligned} \quad (3.18)$$

At higher frequencies, the voltage induced in the coil from the preamp's current noise increases. This frequency dependence presents a challenge when trying to noise match, since we want to noise match for all frequencies.

3.7 Signal-to-Noise Ratio in MPI

As shown in the previous chapter, the signal in the receive coil is dependent on the detection limit of the receive coil. The signal-to-noise ratio of the signal at the sensor is the fundamental sensitivity of an inductive coil.

$$SNR = \frac{\mathbf{B} \frac{d\mathbf{m}}{dt}}{\sqrt{4kTR_{src}BW}} \quad (3.19)$$

The SNR with the noise from the preamplifier included is

$$SNR = \frac{\mathbf{B} \frac{d\mathbf{m}}{dt}}{\sqrt{(4kTR_{src} + e_n^2 + i_n^2 |Z_s|^2)BW}} \quad (3.20)$$

Chapter 4

Optimal Noise Matching

In this chapter, we discuss various techniques to try to match the source impedance to the effective noise resistance of a noisy two port network. Simply adding an additional resistor in series to the source resistance for matching purposes would be an egregious mistake, since that resistor will simply add more noise to the input. The only methods that should be employed are the use of lossless components to transform impedances, e.g. a transformer or LC-matching networks, or the use of averaging to lower the voltage noise at the expense of higher current noise. For each method, we'll discuss how it can achieve noise matching and the limitations of that method.

Another constraint that we have to consider is the bandwidth of the matching network. MPI operates between 20kHz to 2MHz. This translates to designing for a low quality factor in the matching network to achieve optimal matching across the whole bandwidth.

4.1 Transformer Matching

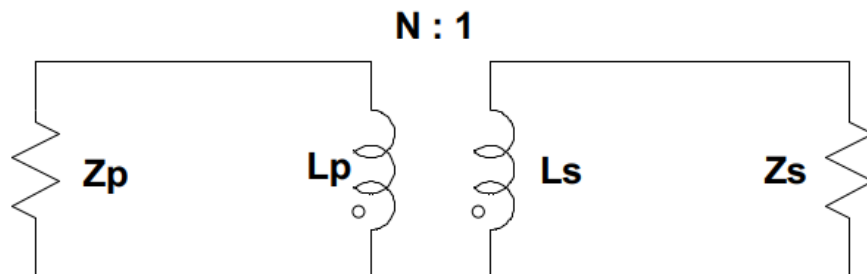


Figure 4.1: Transformer Model with Primary and Secondary Impedances

Transformer operation is described by Faraday's Law of Induction, where the voltage induced on the primary and secondary coils is dependent on the change in flux through the core and the number of turns. Since it is a passive device, the product of $I \cdot V$ is constant on both

sides.

$$\begin{aligned}
 V_p &= -N_p \frac{d\phi}{dt} \\
 V_s &= -N_s \frac{d\phi}{dt} \\
 V_p &= \frac{N_p}{N_s} V_s = N V_s \\
 I_p &= \frac{N_s}{N_p} I_s = \frac{1}{N} I_s
 \end{aligned}
 \tag{4.1}$$

The effective impedance seen from the primary side is

$$Z_p = \frac{V_p}{I_p} = N^2 \frac{V_s}{I_s} = N^2 Z_s
 \tag{4.2}$$

We can therefore choose the turn ratio N to be the matching ratio $M = \frac{Z_p}{Z_s}$

$$N = \sqrt{\frac{Z_p}{Z_s}}
 \tag{4.3}$$

The effect on the noise figure using transformers with a $N : 1$ turn ratio is as follows:

$$NF = 1 + \frac{\frac{e_n^2}{N^2} + N^2 i_n^2 |Z_s|^2}{4kTR_{src}}
 \tag{4.4}$$

The advantage of using a transformer to perform noise matching is that it has a large matching bandwidth and excellent amplitude and phase balance over the matching bandwidth.

The disadvantage when matching with a transformer is that it is actually a lossy component due to copper and core loss; in addition, there are secondary inductances and parasitic capacitances that limit the usage of transformers at microwave frequencies.

4.2 LC Matching Networks

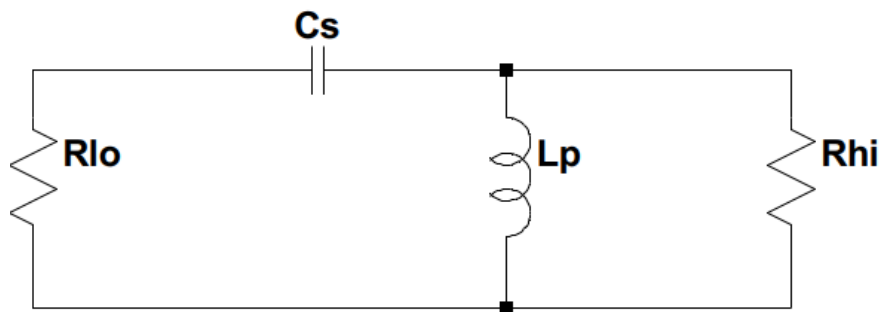


Figure 4.2: Simple LC Matching Network

LC Ladder Matching Networks are great for high-Q matching. For a simple LC match, such as the one shown in Figure 4.2, the quality of the match is dependent on the ratio of the higher impedance and lower impedance.

$$Q = \sqrt{\frac{R_{hi}}{R_{lo}} - 1} \quad (4.5)$$

For an AC coupled LC match at a center frequency f_c , the design equations are as follows:

$$\begin{aligned} X_p &= \frac{R_{hi}}{Q} \\ L_p &= \frac{X_p}{2\pi f_c} \\ X_s &= \frac{X_p}{1 + Q^2} \\ C_s &= \frac{1}{X_s \cdot 2\pi f_c} \end{aligned} \quad (4.6)$$

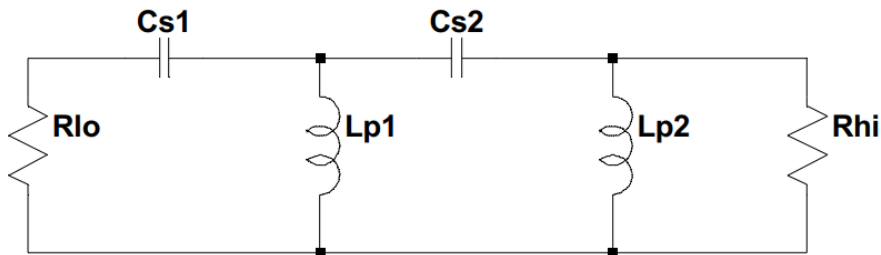


Figure 4.3: Two Section LC Network

More complex LC matching networks can be employed to design for a specific Q. While Tee and Pi networks allow for more narrowband matches with higher Q, multi-section LC matching allows for wideband, lower Q matching by choosing intermediate impedances. An example of a multi-section LC matching network is shown in Figure 4.3. The minimum Q for a two section network is when the optimal intermediate impedance is

$$R_{int,opt} = \sqrt{R_{hi} \cdot R_{lo}} \quad (4.7)$$

This can be generalized to a N-section LC network where the optimal intermediate impedances between sections is a geometric progression from the previous stage impedance. This leads to the optimal lowest Q of

$$Q_{min} = \sqrt{\left(\frac{R_{hi}}{R_{lo}}\right)^{1/N} - 1} \quad (4.8)$$

The advantages of using the multi-section LC network is being able to achieve a larger matched bandwidth. There is also a minimum number of sections N such that the insertion

loss due to lossy components is also minimized. The disadvantage of using a multi-section LC network at a low center frequency is the use of unreasonably sized component values such as large inductances.

4.3 Parallel LNA Devices

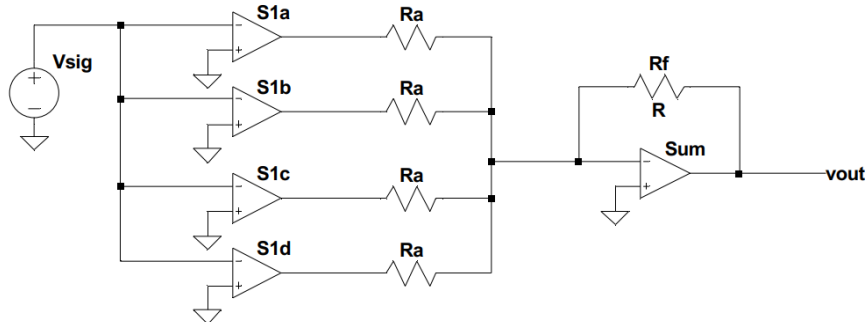


Figure 4.4: Summing Amplifier

In the case where parallel LNAs are used as the preamplifier, we can take the sum of the outputs of each LNA as shown in Figure 4.4, which is similar to taking an average. We can increase SNR by averaging our signal since the variance of noise of the average of N noisy observations is a factor N smaller. The variance of a white gaussian noise process X can be described in the following equation:

$$\text{Var}\left(\frac{1}{N} \sum_i^N X_i\right) = \frac{1}{N^2} \{N \text{Var}(X)\} = \frac{1}{N} \text{Var}(X) \quad (4.9)$$

Assuming the signal is constant as we average, then the mean of the signal portion of the output of the summing amplifier is just the signal. However, we also effectively add the current noise sources of the N parallel devices, which means that our effective current noise variance is multiplied by N .

The Noise Figure for this case can be described in the following equation:

$$NF = 1 + \frac{\frac{e_n^2}{N} + N i_n^2 |Z_s|^2}{4kTR_{src}} \quad (4.10)$$

The advantage of averaging using parallel amplifiers is very low voltage noise and a wide bandwidth match. However, this comes at the cost of very high power consumption, higher current noise and bandwidth of the amplifier. The bandwidth of the amplifier decreases by a factor of N since the system is now loaded by N input capacitances. This should not be a concern if the input capacitance is sufficiently small and the bandwidth of the LNA is sufficiently large.

4.4 Bandwidth Limits on Matching Networks

To understand the the limits on how much bandwidth our matching network covers, we go back to electromagnetic theory. When the source and load impedances of a traveling EM wave are not matched there is a reflected wave back to the source. The reflection coefficient from the source to the load is defined to be

$$\Gamma(\omega) = \frac{Z_L - Z_S}{Z_L + Z_S} \quad (4.11)$$

Zheng et al uses the results from Fano-Bode to show that for an inductive source and reflection coefficient $\Gamma(\omega)$ [18]:

$$\int_0^\infty \ln \left| \frac{1}{\Gamma(\omega)} \right| d\omega \leq \frac{\pi \cdot R_{src}}{L_{src}} \quad (4.12)$$

$$\left| \Gamma(\omega) \right|^2 = \frac{(NF - 1) \cdot 2kT - e_n i_n}{(NF - 1) \cdot 2kT + e_n i_n} \quad (4.13)$$

Assuming a constant reflection coefficient across the entire spectrum, then it can be shown that the absolute maximum matched bandwidth under ideal conditions is:

$$\Delta\omega \leq \frac{2\pi R_{src}}{L_{src}} \frac{kT \cdot (NF - 1)}{e_n \cdot i_n} \quad (4.14)$$

The only design parameter that can be reasonably tuned to increase the matched bandwidth is the $e_n i_n$ product of our preamplifier. Increasing R_{src} , T , or NF would only add noise to the system and degrade SNR. Decreasing L_{src} may seem like an option to increase the matched bandwidth, but a smaller L_{src} would mean a weaker signal since the sensitivity of the detector coil scales with the number of turns.

Chapter 5

Ultra Low Noise Preamplifier Analysis and Design

In this chapter we will discuss methods to achieve low input referred noise voltage and current.

5.1 Device Choices

The input stage of our amplifier was chosen to be comprised of N-channel junction field effect transistors (JFET). JFETs have the desirable qualities of low voltage noise, low current noise, high transconductance gain, and high input impedance. One disadvantage is that their input capacitance is fairly high (tens of picoFarads), which means that given a large inductance, the resonant frequency would be lower. We want our resonant frequency to be out of band and our passband gain to be fairly flat, since MPI, unlike MRI, does not utilize resonance and is broadband (20 kHz to 2-4 MHz).

5.2 Cascode Topology

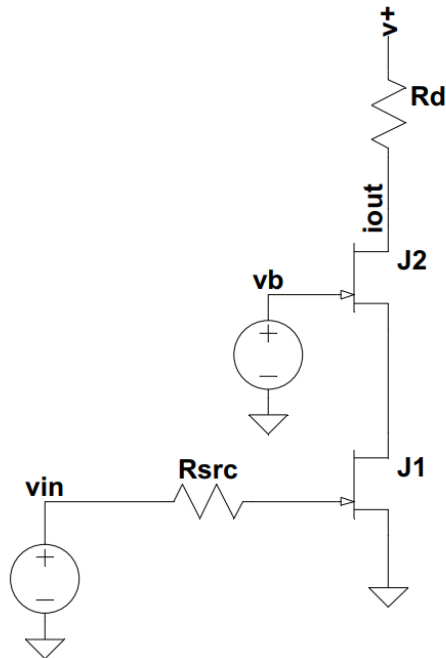


Figure 5.1: JFET Cascode

Cascoding devices improves the gain and output resistance of the amplifier while minimally contributing noise since the cascode device on top experiences source degeneration by common source device on the bottom, boosting the output resistance by a factor of $g_m r_o$. Because the cascode device current noise is degenerated, the output current noise due to the cascode device is

$$i_{out} = \frac{1}{1 + g_m r_o} i_{n,d} \approx 0 \text{ for } g_m r_o \gg 1 \quad (5.1)$$

The contribution of noise due to the cascode device compared to the noise of the common source device is negligible, so we can essentially ignore it.

5.3 Negative Feedback Effects on Noise

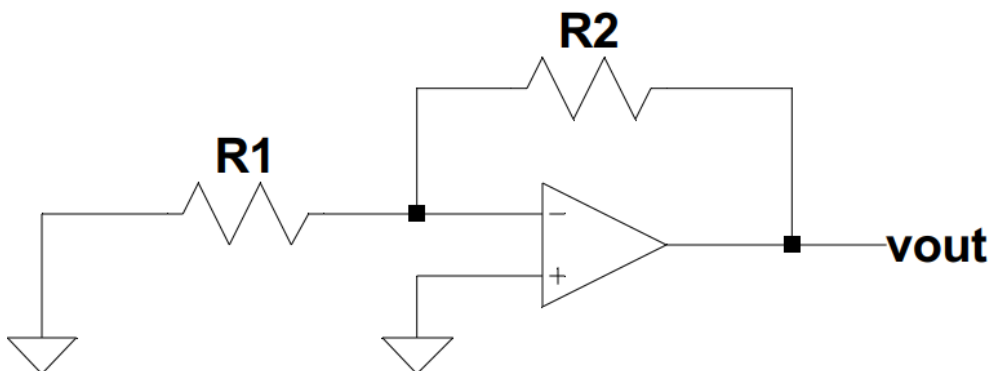


Figure 5.2: Shunt-Series Resistive Feedback

While resistive feedback networks contribute noise to the output due to thermal noise, feedback is essential for precise and controllable gain. The approximate noise added for a standard shunt-series resistive feedback network like the one shown in Figure 5.2 can be calculated as follows for a non-inverting amplifier configuration with a gain of $\frac{R_1+R_2}{R_1}$.

The input referred noise of the thermal noise due to R_2 is

$$\begin{aligned}\overline{V_{out,n,R_2}^2}/\delta f &= 4kTR_2 \\ \overline{V_{in,n,R_2}^2}/\delta f &= 4kTR_2\left(\frac{R_1}{R_1+R_2}\right)^2 \approx 0 \text{ for } R_2 \gg R_1\end{aligned}\tag{5.2}$$

The input referred noise of the thermal noise due to R_1 is

$$\begin{aligned}\overline{V_{out,n,R_1}^2}/\delta f &= 4kTR_1\left(\frac{R_2}{R_1}\right)^2 \\ \overline{V_{in,n,R_1}^2}/\delta f &= 4kTR_1\left(\frac{R_2}{R_1}\right)^2\left(\frac{R_1}{R_1+R_2}\right)^2 = 4kTR_1\left(\frac{R_2}{R_1+R_2}\right)^2 \\ &\approx 4kTR_1 \text{ for } R_2 \gg R_1\end{aligned}\tag{5.3}$$

The noise contribution of R_2 is negligible if the gain is large and the contribution of R_1 is negligible if R_1 itself is small. This suggests that designing the feedback network requires $R_2 \gg R_1$ and R_1 to be small.

5.4 Proposed Design: AC Analysis

For our first stage, we used a JFET cascode AC coupled with a TIA shown in Figure 5.3.

The transconductance gain of the cascode is approximately

$$G_m = \frac{I_{out}}{V_{in}} = g_m\tag{5.4}$$

The passband transimpedance gain of the TIA is

$$R_{ac} = \frac{V_{out}}{I_{in}} = R_t\tag{5.5}$$

Combined, the overall gain of the stage is then

$$A_{ol} = \frac{V_{out}}{V_{in}} = g_m R_t\tag{5.6}$$

The open loop gain for this design is large because the g_m for the JFET we used is approximately 35 mS, which, when combined with an R_t of 100k, gives us an open loop gain of

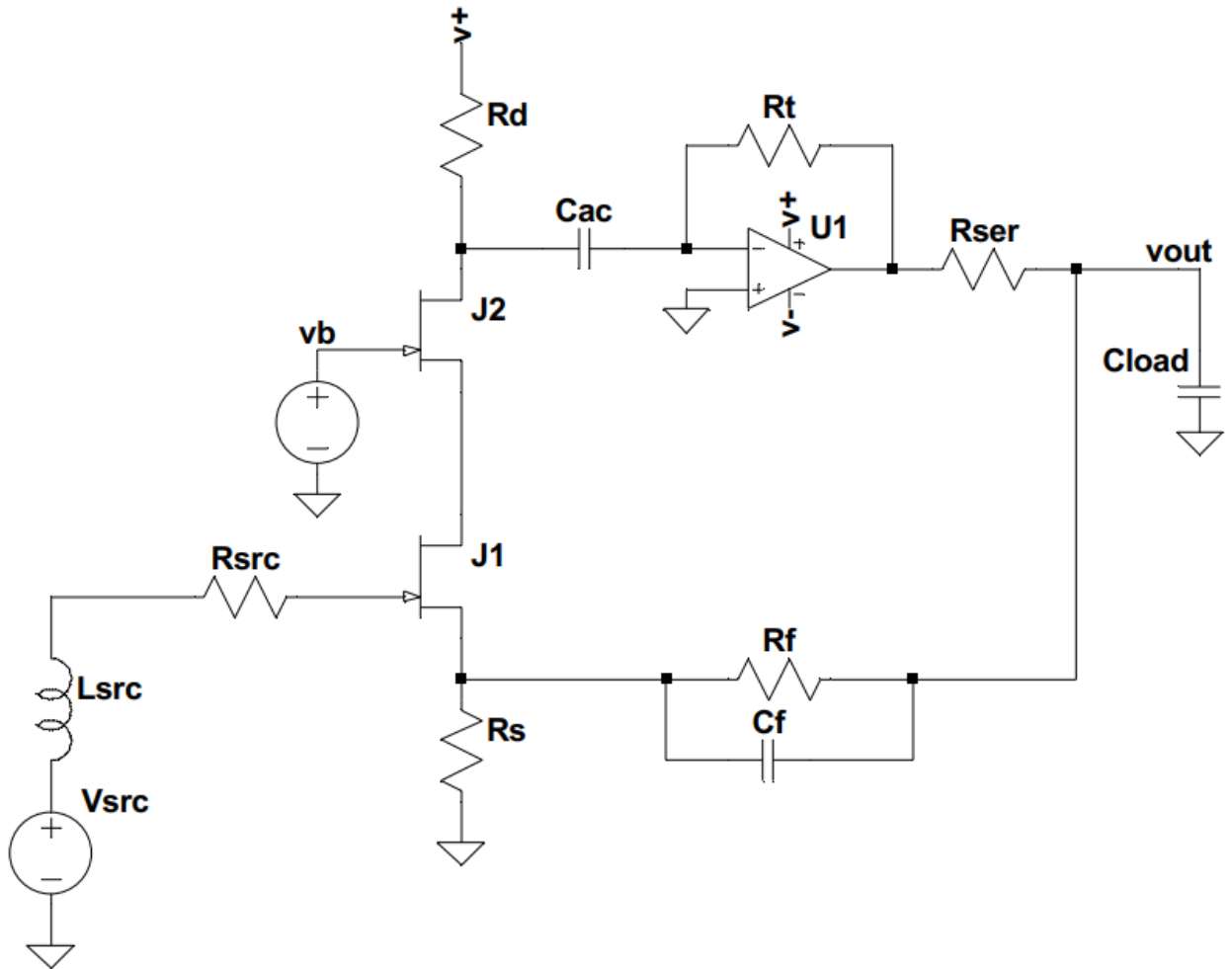


Figure 5.3: Proposed Preamplifier Design

3500. However, to keep the gain precise, we use a feedback network with $R_s = 5 \Omega$ and $R_f = 100 \Omega$.

$$\beta = \frac{R_s}{R_s + R_f} = \frac{5}{5 + 100} = \frac{1}{21} \quad (5.7)$$

Now the closed loop gain of the entire stage is

$$A_{cl} = \frac{A_{ol}}{1 + A_{ol}\beta} \approx \frac{1}{\beta} = 1 + \frac{R_f}{R_s} = 21 \quad (5.8)$$

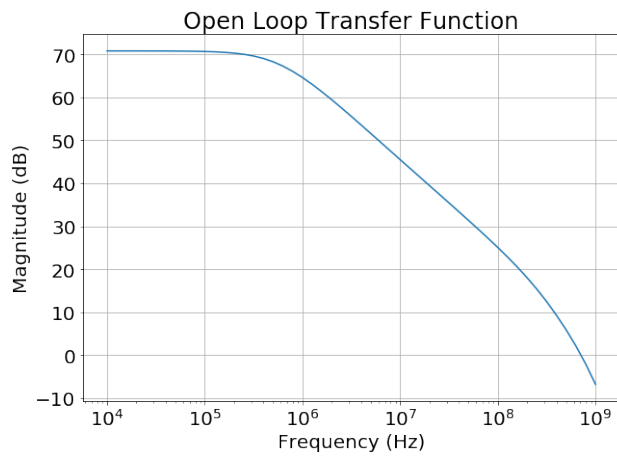


Figure 5.4: Open Loop Gain

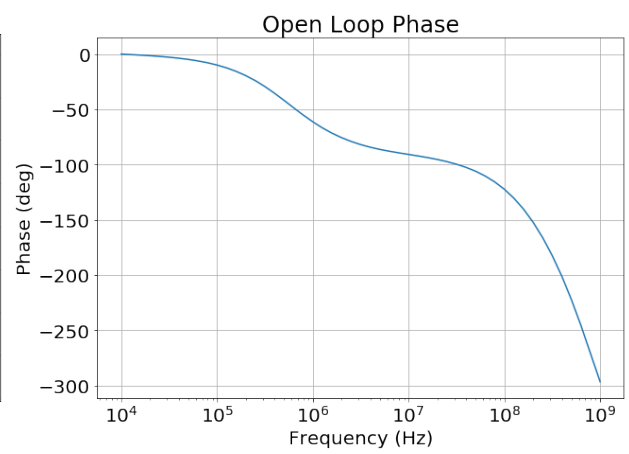


Figure 5.5: Open Loop Phase

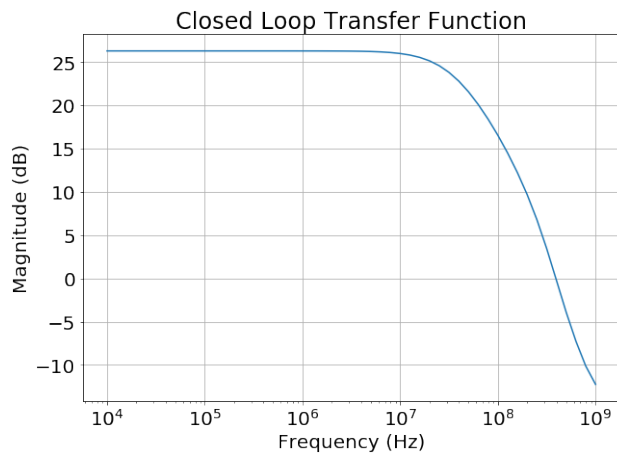


Figure 5.6: Closed Loop Gain

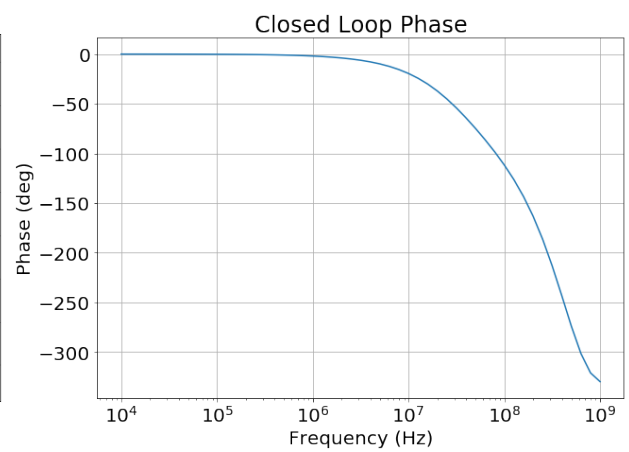


Figure 5.7: Closed Loop Phase

Using SPICE, we confirmed the open loop and closed loop gains in Figures 5.4-5.5 and 5.6-5.7 respectively. The open loop passband gain of the preamplifier is 70.8 dB. The closed loop passband gain of the preamplifier is 26.3 dB. The calculated open loop and closed loop gain was 70.88 dB and 26.44 dB. The simulated closed loop gain is 0.53% off from the calculated closed loop gain.

5.5 Proposed Design: Stability Analysis

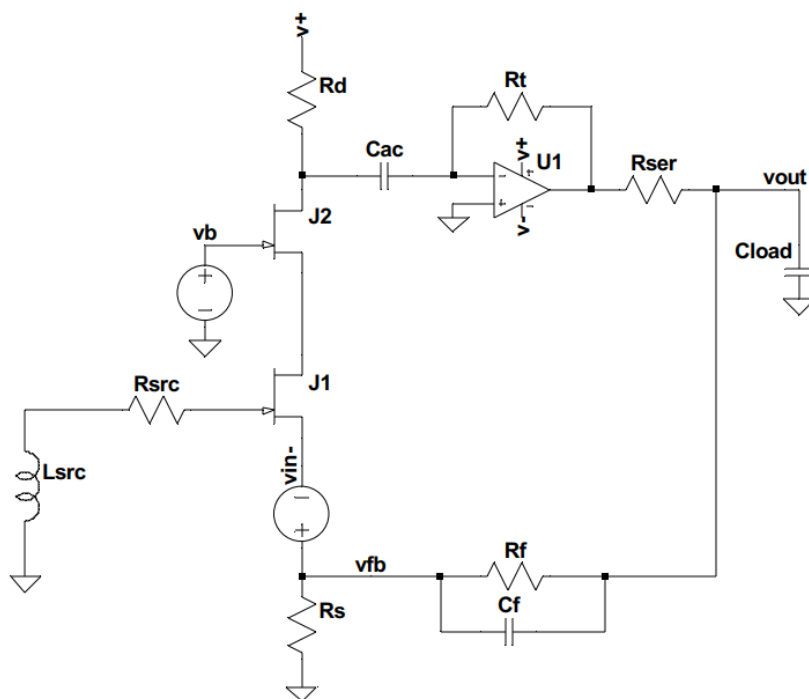


Figure 5.8: Loop Gain Stability Testbench

To confirm that the amplifier was stable for all frequencies, we used the return ratio method where we turned off all independent sources and then inserted a source in the feedback path, shown in Figure 5.8. We then measured the return ratio by finding the transfer function of the voltage at the feedback point over the voltage at the inverting input.

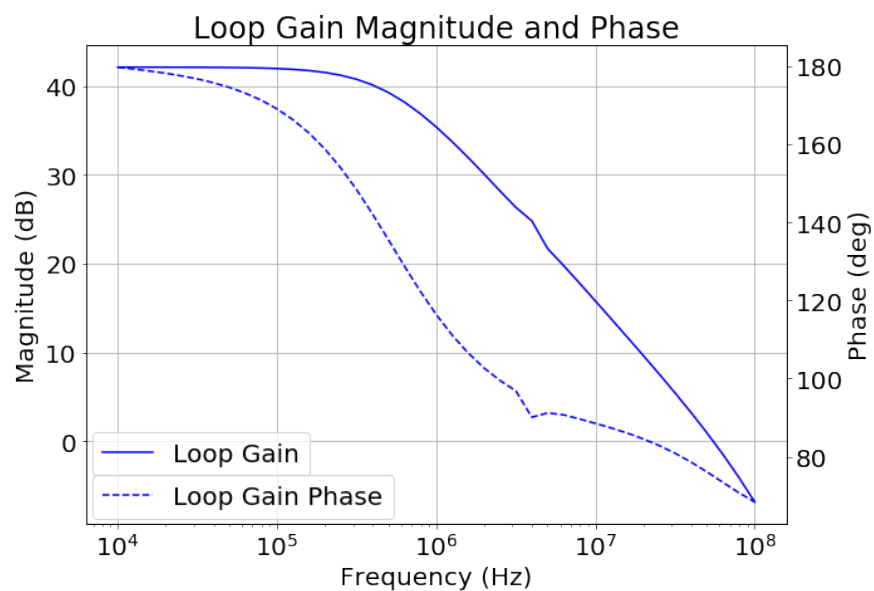


Figure 5.9: Loop Gain Stability

Using SPICE, we confirmed the circuit's stability in Figure 5.9. At unity gain frequency, the phase margin is 75 degrees, suggesting that the circuit is stable.

5.6 Proposed Design: Noise Analysis

The output voltage noise variance of the open loop design is calculated as follows:

$$\begin{aligned} \overline{V_{n,out}^2} &= \overline{V_{n,R_{ser}}^2} + (g_m R_t)^2 \overline{V_{n,R_{src}}^2} + \left(\frac{R_t}{R_d}\right)^2 \overline{V_{n,R_d}^2} + \overline{V_{n,R_t}^2} \\ &+ \left(\frac{R_t + R_d}{R_d}\right)^2 e_n^2 + R_t^2 i_n^2 + R_t^2 i_d^2 \end{aligned} \quad (5.9)$$

i_d is the drain thermal noise of the common source device, e_n is the voltage noise of the opamp, i_n is the current noise of the opamp. We divided by the open loop gain $g_m R_t$ squared to get the input referred voltage noise variance.

$$\begin{aligned} \overline{V_{n,in}^2} &= \left(\frac{1}{g_m R_t}\right)^2 \overline{V_{n,R_{ser}}^2} + \overline{V_{n,R_{src}}^2} + \left(\frac{1}{g_m R_d}\right)^2 \overline{V_{n,R_d}^2} + \left(\frac{1}{g_m R_t}\right)^2 \overline{V_{n,R_t}^2} \\ &+ \left(\frac{1}{g_m R_d}\right)^2 e_n^2 + \left(\frac{1}{g_m}\right)^2 (i_n^2 + i_d^2) \end{aligned} \quad (5.10)$$

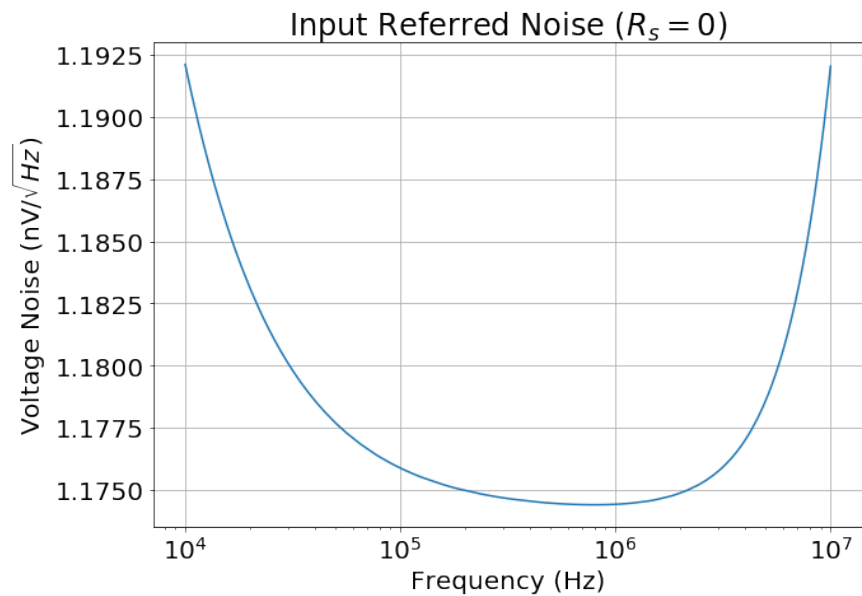


Figure 5.10: Input Referred Noise with Zero Source Resistance

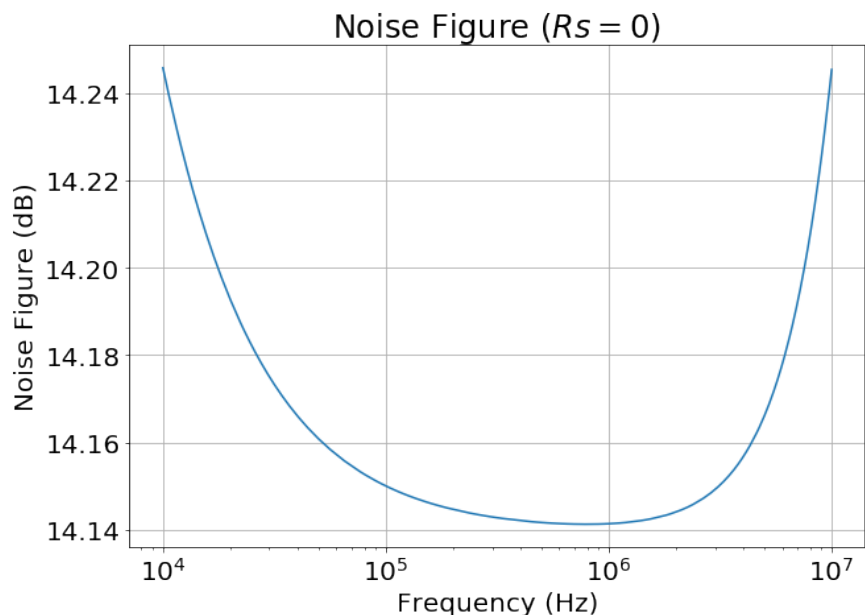


Figure 5.11: Noise Figure with No Matching

In Spice, we performed a noise analysis with zero source resistance and plotted the input referred noise shown in Figure 5.10. We also added in the source impedance and plotted the noise figure with no noise matching done in Figure 5.11. The noise figure without matching is roughly 14.2 dB throughout the band.

To accurately characterize the noise of our proposed preamplifier, we calculated the voltage and current noise densities in the passband. In SPICE we swept different values of the source resistance and stored the input referred noise voltage. To find e_n and i_n we only need 2 points, which can be done with $R_{src} = 0$ and a large R_{src} but we chose to sweep several values of R_{src} . From these values we were able to use Least Squares Regression to get the best estimate for e_n and i_n

$$\begin{bmatrix} 1 & R_{src,1}^2 \\ \vdots & \\ 1 & R_{src,n}^2 \end{bmatrix} \begin{bmatrix} e_n^2 \\ i_n^2 \end{bmatrix} = \begin{bmatrix} v_{n,i,tot,1}^2 - 4kTR_{src,1} \\ \vdots \\ v_{n,i,tot,n}^2 - 4kTR_{src,n} \end{bmatrix} \quad (5.11)$$

From the least squares solution, $e_n = 1.19 \text{ nV}/\sqrt{\text{Hz}}$ and $i_n = 0.110 \text{ pA}$ at 200 kHz. The noise power and resistance is then

$$\begin{aligned} p_n &= e_n i_n = 1.32 \cdot 10^{-22} \text{ W/Hz} \\ R_n &= e_n / i_n = 10.71 \text{ k}\Omega \end{aligned} \quad (5.12)$$

5.7 Proposed Design: Noise Matching

As a first pass attempt at noise matching 10.71 k Ω to 5 Ω , we used an ideal transformer with a turns ratio of 1 : 2142 This yields an input referred noise shown in Figure 5.12. We calculated the noise figure of this matched preamplifier by dividing the input referred noise voltage by the contribution of thermal noise due to the source resistance, shown in Figure 5.13. From 30 kHz to 300 kHz, we achieve a noise figure below 0.5 dB. From 20 kHz to 1 MHz, the noise figure is below 1.5 dB. The transformer is unrealistic because of the unreasonable turns ratio and the fact that the self resonance frequency for an unideal version of this would probably be in-band. We discuss another attempt in the next paragraph.

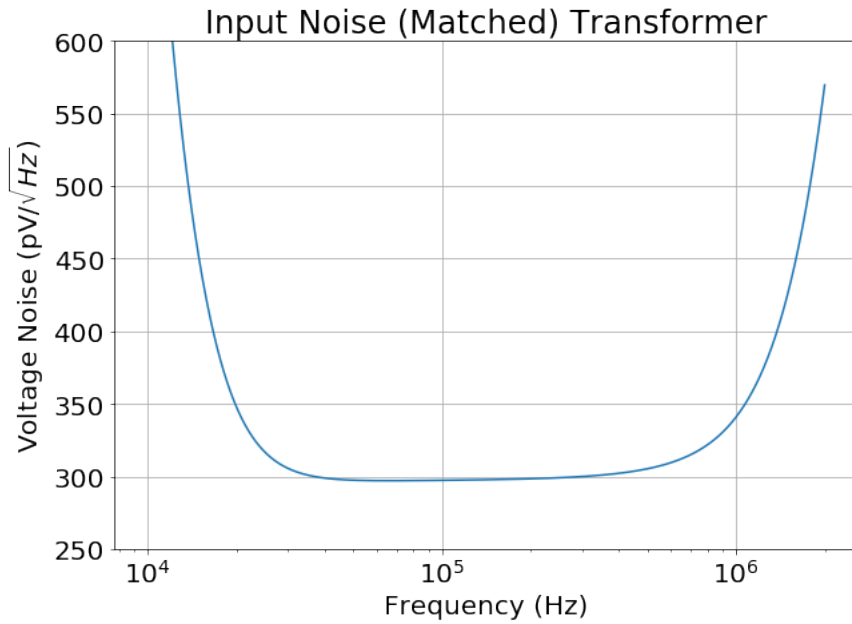


Figure 5.12: Input Referred Noise with Transformer Matching

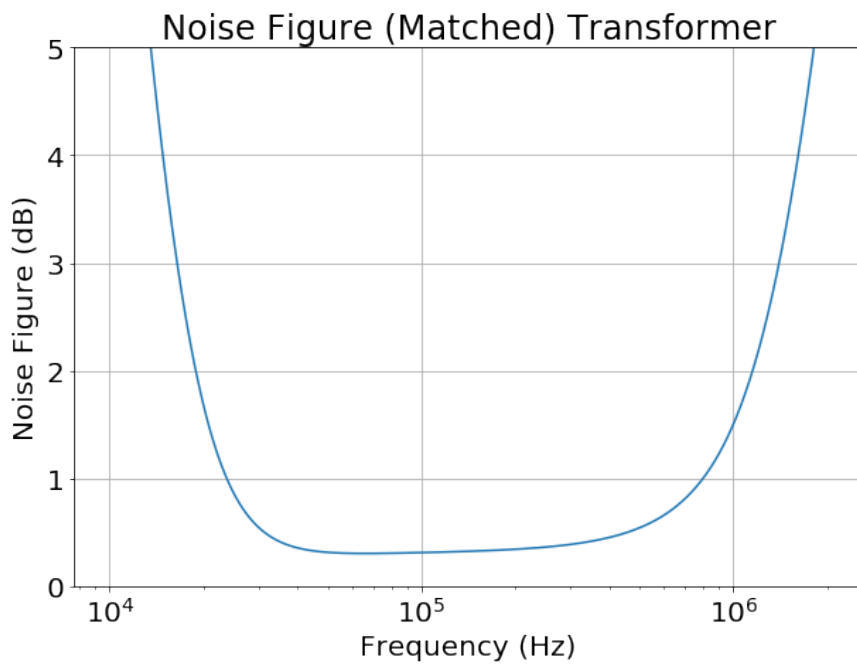


Figure 5.13: Noise Figure with Transformer Matching

Since the transformer turn ratio is unrealistic, we make another attempt by using the parallel preamplifier configuration in conjunction with the matching transformer. We used 4 parallel preamps along with an ideal transformer with a turns ratio of 1:100. This yields an input referred noise shown in Figure 5.14. We calculated the noise figure of this matched preamplifier by dividing the input referred noise voltage by the contribution of thermal noise due to the source resistance, shown in Figure 5.15. From 300 kHz to 800 kHz, we achieve a noise figure below 0.8 dB. From 30 kHz to 1 MHz, the noise figure is below 2 dB.

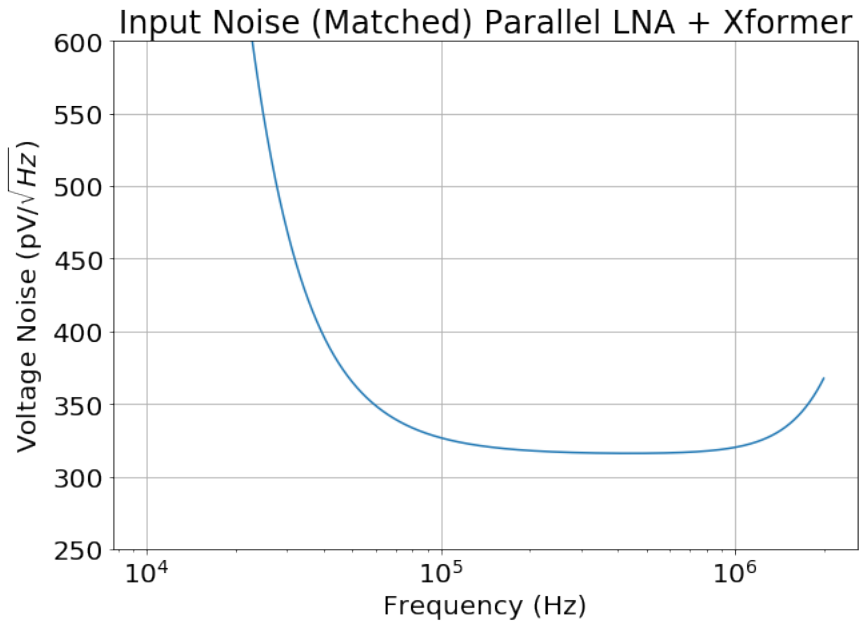


Figure 5.14: Input Referred Noise with Parallel Preamps and Transformer Matching

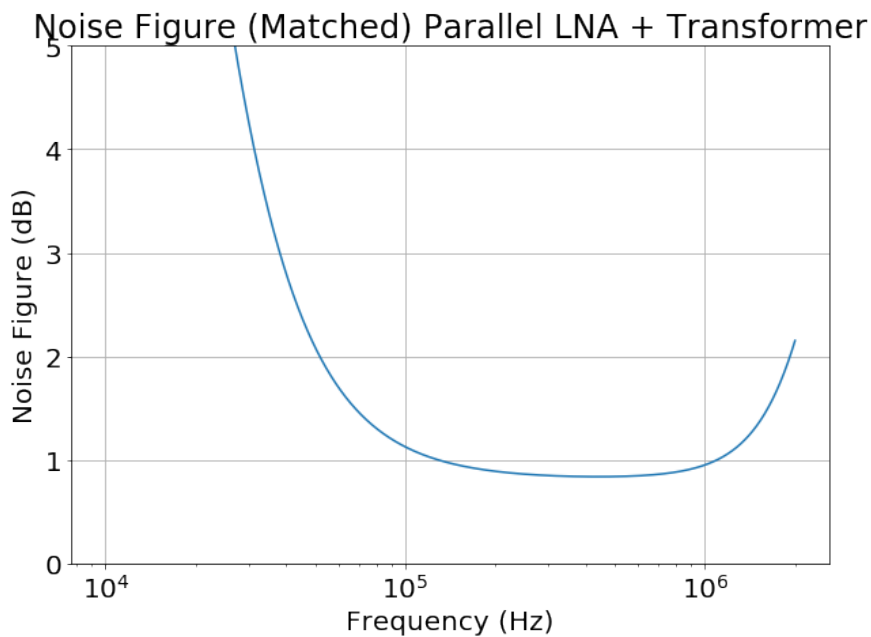


Figure 5.15: Noise Figure with Parallel Preamps and Transformer Matching

5.8 Comparison to Previous Preamplifiers

In this section we compare our proposed design to the previous preamplifiers used in BISL. We use a Stanford Research Systems SR560 Low Noise Preamplifier. Using the same least squares regression to solve for e_n and i_n of the SR560, we get the following noise metrics. I also use noise figure metrics from Zheng et al. [18]

SR560

$$p_n = e_n i_n = 4.83 \cdot 10^{-21} \text{ W/Hz} \quad (5.13)$$

$$R_n = e_n / i_n = 2.98 \text{ k}\Omega$$

Performance Metric	Proposed	SR560
p_n (W/Hz)	$2.7 \cdot 10^{-22}$	$4.83 \cdot 10^{-21}$
R_n (Ω)	10.71k	2.98k
NF_{no match} (dB)	14.2	23
NF_{min,ideal} (dB)	0.07	2.04
NF_{min,acheivable} (dB)	0.75	-
Gain (V/V)	20.6	Variable
Common Mode Rejection Ratio (dB)	0	40
Bandwidth (Closed Loop) (Hz)	36 MHz	1 MHz
Power Consumption (W)	1.186	6

Table 5.1: Noise Performance Comparison Table. We see an improvement in Noise Figure from 23 dB to 14.2 dB (8.8 dB improvement in SNR) with even further improvements with noise matching techniques.

We also compare the power consumption, common mode rejection ratio (CMRR) and bandwidth. Since we have a single-ended input preamplifier, the common mode rejection ratio is 0 dB. Future works will consider making the input differential to increase CMRR. Right now common mode mitigation techniques include operating the scanner and preamplifier in a Faraday cage and using twisted pair wires.

Chapter 6

Conclusion

6.1 Motivation and Big Picture

It may be some time until MPI reaches body noise dominance using perhaps high temperature superconducting receiver coils (HTS coils for MRI) or SQUIDs [28]. For now we can at least design the preamplifier such that MPI is receive coil noise dominated. As the noise figure of MPI receive systems continue to improve, the detection sensitivity decreases to a few dozen nanograms of iron tracer per voxel. This improves confidence in applications of MPI such as gut bleed, immunotherapy (white blood cell (WBC) counting for cancer detection), red blood cell tracking, and stem cell tracking [4, 7, 8]. All these applications require single cell tracking and all suffer from poor SNR and variable labeling efficiency using current state of the art imaging techniques. A noise figure improvement from 2 dB to 0.1 dB would go a long way to deal with these issues and help us reach MPI's physical limit of detecting 1-5 cells.

6.2 Future Work

Future work that I would like to consider is utilizing more complex matching networks to achieve the minimum achievable noise figure and helping the lab implement HTS coils for the scanner.

Another way to achieve low noise figure and improve detection sensitivity for Magnetic Particle Imaging would be to make an application specific integrated circuit. Something I would also like to consider is having access to technology nodes that would allow me to design a custom low noise preamplifier chip instead of relying on off-the-shelf components that meet a certain noise, gain and bandwidth specification.

Bibliography

- [1] Gleich, B. and Weizenecker, J. (2005). Tomographic imaging using the nonlinear response of magnetic particles. *Nature* 435, 12141217.
- [2] Goodwill, P., R. M. Ferguson, E. Yu, R. Orendorff, Bo Zheng, Kuan Lu, D. Hensley, et al. 2015. In Vivo and Ex Vivo Experimental MPI Angiography with High Selection Field Strength and Tailored SPIO Nanoparticles. In *Magnetic Particle Imaging (IWMPI), 2015 5th International Workshop on*, 11. ieeexplore.ieee.org.
- [3] Ludewig, P., Gdaniec, N., Sedlacik, J., Forkert, N.D., Szwargulski, P., Graeser, M., Adam, G., Kaul, M.G., Krishnan, K.M., Ferguson, R.M., et al. (2017). Magnetic Particle Imaging for Real-Time Perfusion Imaging in Acute Stroke. *ACS Nano* 11, 1048010488.
- [4] Zheng, B., von See, M.P., Yu, E., Gunel, B., Lu, K., Vazin, T., Schaffer, D.V., Goodwill, P.W., and Conolly, S.M. (2016). Quantitative Magnetic Particle Imaging Monitors the Transplantation, Biodistribution, and Clearance of Stem Cells In Vivo. *Theranostics* 6, 291301
- [5] Zhou, X.Y., Jeffris, K.E., Yu, E.Y., Zheng, B., Goodwill, P.W., Nahid, P., and Conolly, S.M. (2017). First in vivo magnetic particle imaging of lung perfusion in rats. *Phys. Med. Biol.* 62, 35103522.
- [6] Orendorff, R., Peck, A.J., Zheng, B., Shirazi, S.N., Matthew Ferguson, R., Khandhar, A.P., Kemp, S.J., Goodwill, P., Krishnan, K.M., Brooks, G.A., et al. (2017). First in vivo traumatic brain injury imaging via magnetic particle imaging. *Phys. Med. Biol.* 62, 35013509.
- [7] Zhou, XY, (2018) Magnetic Particle Imaging for Radiation-Free, Sensitive and High-Contrast Vascular Imaging and Cell Tracking, *Current Opinion in Chemical Biology*.
- [8] Yu, E.Y., Chandrasekharan, P., Berzon, R., Tay, Z.W., Zhou, X.Y., Khandhar, A.P., Ferguson, R.M., Kemp, S.J., Zheng, B., Goodwill, P.W., et al. (2017). Magnetic Parti-

- cle Imaging for Highly Sensitive, Quantitative, and Safe in Vivo Gut Bleed Detection in a Murine Model. ACS Nano 11, 1206712076.
- [9] Townsend, David W. (2008), "Combined PET/CT: the historical perspective", Semin Ultrasound CT MR, 29 (4): 232235,
- [10] MartBonmati, L. , Sopena, R. , Bartumeus, P. and Sopena, P. (2010), Multimodality imaging techniques. Contrast Media Mol Imaging, 5: 180-189. doi:10.1002/cmml.393
- [11] D. Hoult, The principle of reciprocity in signal strength calculations A mathematical guide, Concept Magn. Res., vol. 12, no. 4, pp. 173187, 2000.
- [12] P. W. Goodwill and S. M. Conolly, *The X-Space Formulation of the Magnetic Particle Imaging Process: 1-D Signal, Resolution, Bandwidth, SNR, SAR, and Magnetostimulation*, in IEEE Transactions on Medical Imaging, vol. 29, no. 11, pp. 1851-1859, Nov. 2010. doi: 10.1109/TMI.2010.2052284
- [13] Lu K, Goodwill PW, Saritas EU, Zheng B, Conolly SM. Linearity and Shift Invariance for Quantitative Magnetic Particle Imaging. IEEE transactions on medical imaging. 2013;32(9):10.1109/TMI.2013.2257177. doi:10.1109/TMI.2013.2257177.
- [14] E. U. Saritas, P. W. Goodwill, G. Z. Zhang and S. M. Conolly, "Magnetostimulation Limits in Magnetic Particle Imaging," in IEEE Transactions on Medical Imaging, vol. 32, no. 9, pp. 1600-1610, Sept. 2013. doi: 10.1109/TMI.2013.2260764
- [15] Croft, Laura R., Patrick W. Goodwill, and Steven M. Conolly. 2012. Relaxation in X-Space Magnetic Particle Imaging. IEEE Transactions on Medical Imaging 31 (12): 233542.
- [16] Goodwill, P. W., A. Tamrazian, L. R. Croft, C. D. Lu, E. M. Johnson, R. Pidaparathi, R. M. Ferguson, A. P. Khandhar, K. M. Krishnan, and S. M. Conolly. 2011. Ferrohydrodynamic Relaxometry for Magnetic Particle Imaging. Applied Physics Letters 98 (26). AIP Publishing: 262502.
- [17] Tay ZW, Goodwill PW, Hensley DW, Taylor LA, Zheng B, Conolly SM. *A High-Throughput, Arbitrary-Waveform, MPI Spectrometer and Relaxometer for Comprehensive Magnetic Particle Optimization and Characterization*. Scientific Reports. 2016;6:34180.
- [18] B. Zheng et al., *Optimal Broadband Noise Matching to Inductive Sensors: Application to Magnetic Particle Imaging*, in IEEE Transactions on Biomedical Circuits and Systems, vol. 11, no. 5, pp. 1041-1052, Oct. 2017.

- [19] H. A. Wheeler, "Simple Inductance Formulas for Radio Coils," in Proceedings of the Institute of Radio Engineers, vol. 16, no. 10, pp. 1398-1400, Oct. 1928.
- [20] Schenck, J. F. (1996), The role of magnetic susceptibility in magnetic resonance imaging: MRI magnetic compatibility of the first and second kinds. *Med. Phys.*, 23: 815-850. doi:10.1118/1.597854
- [21] H. A. Wheeler, "Formulas for the Skin Effect," in Proceedings of the IRE, vol. 30, no. 9, pp. 412-424, Sept. 1942. doi: 10.1109/JRPROC.1942.232015
- [22] G. Grandi, M. K. Kazimierczuk, A. Massarini and U. Reggiani, "Stray capacitances of single-layer air-core inductors for high-frequency applications," Industry Applications Conference, 1996. Thirty-First IAS Annual Meeting, IAS '96., Conference Record of the 1996 IEEE, San Diego, CA, 1996, pp. 1384-1388 vol.3. doi: 10.1109/IAS.1996.559246
- [23] Sears, F. W. Faraday's law and Ampere's law. *American Journal of Physics*, v. 31, p. 439-443, 1963
- [24] Macovski, A. (1996), *Noise in MRI*. *Magn. Reson. Med.*, 36: 494-497.
- [25] J.B. Johnson, "Thermal Agitation of Electricity in Conductors", *Phys. Rev.*, 32, 97-109, (1928)
- [26] H. T. Friis, *Noise Figures of Radio Receivers*, in Proceedings of the IRE, vol. 32, no. 7, pp. 419-422, July 1944.
- [27] F. A. Levinzon, *Noise of the JFET amplifier*, in *IEEE Transactions on Circuits and Systems I: Fundamental Theory and Applications*, vol. 47, no. 7, pp. 981-985, Jul 2000.
- [28] Clarke J: SQUID fundamentals. In *SQUID Sensors: Fundamentals, Fabrication and Applications*. Edited by Weinstock H. Dordrecht: Kluwer Academic Press; 1996:1-62. Comprehensive, introductory overview of theory and practice of SQUIDS, SQUID-based instruments, and applications. Many references. The entire book represents a complete, up-to-date overview of all aspects of SQUIDS.